Journal of Materials Chemistry A

ROYAL SOCIETY OF CHEMISTRY

PAPER

View Article Online
View Journal | View Issue

Cite this: J. Mater. Chem. A, 2026, 14, 22672

Unveiling the potential of lignin-derived hard carbon as an anode material for Li- and post-Li-ion batteries: a computational investigation

Jafar Azizi,[a] Axel Groß *[a] and Holger Euchner [b]

Hard carbon is one of the most promising anode materials for post-Li-ion batteries; however, the relationship between the precursor material and performance is still hardly understood. In this work, we present a theoretical investigation of hard carbon anode materials derived from lignin, one of the most prevalent biomass materials. Using density functional theory-based calculations, the formation of several lignin-derived hard carbon structures at different temperatures was investigated, yielding amorphous structures with different morphologies. We observe a significant impact of the preparation routine on the resulting hard carbon structure and the corresponding properties. The created materials show a robust morphology and an increased capacity (AMC_n, $n < 6$) as compared to pristine graphite. While unsaturated carbon bonds may result in unfavorable insertion potentials, preparation routes that decrease the number of these bonds yield materials that show promising properties for anode applications in Li-, Na-, and K-ion batteries.

Received 13th January 2026
Accepted 12th April 2026

DOI: 10.1039/d6ta00336b

rsc.li/materials-a

1 Introduction

When it comes to grid-scale energy storage, sodium-ion batteries (NIBs) are becoming the most viable option for beyond lithium-ion batteries (LIBs), which is mostly due to their comparable mechanism and cheaper cost.[1–4] While graphite-based anodes – the standard for Li-ion batteries – are not suitable for NIBs, numerous NIB anode materials were investigated.[5–8] A cutting-edge anode material for NIBs is hard carbon (HC),[9–13] which has gained increased attention in battery research. While Li storage in graphite and other graphite-based materials for LIBs is dominated by intercalation in the graphitic domains, for HC, the storage mechanism is somewhat different. According to the original work by Dahn *et al.*,[14] hard carbons have a high degree of cross-linking and a very complex structure made up of a mixture of pseudo-graphitic domains and amorphous regions, and can be described by the widely acknowledged house of cards model. The latter one and modifications thereof explain how alkali metals (AMs) are stored in HC compounds,[15–18] starting with the adsorption on defects and edges at the surface. This is followed by the intercalation between often defective carbon planes of small graphitic domains.[19] Finally, in the plateau region of the discharge curve, at low potential, the filling of micro- and nano-pores with creation of pseudometallic AM clusters is responsible for a significant fraction of the capacity.[20]

Apart from the exact microstructure of HC anodes, which can strongly affect the storage process, interface effects and electrolyte composition can also have a significant impact.[21–25] For instance, it was shown that the amount and type of solvents and salts can significantly affect the electrochemical performance of AM-ion batteries.[26–28] This is due to the complex interaction between the electrode and electrolyte, which is responsible for the formation of the solid–electrolyte interface (SEI). Graphite, for instance, was found to undergo exfoliation due to solvent intercalation,[29,30] whereas in HC, this is not an issue. Furthermore, HC shows better compatibility with some commonly used electrolytes, such as ether- or carbonate-based electrolytes.[25,31,32] The preparation of HC from biomass exhibits great promise, due to its significantly lower price as compared to graphite, which is moreover combined with a high sustainability.[33–35] A part of the biomass, which corresponds to lignin,[36–38] shows interesting properties as a raw material for HC generation. However, it should be pointed out that the amount of lignin in biomass available for the preparation of HC varies according to the raw material used in the pyrolysis process. One of the natural fibers with a high lignin content is coconut coir fiber with an average lignin content of 46%.[39,40] In fact, about 30% of the organic carbon compounds in the biosphere corresponds to lignin, making it the second most prevalent terrestrial bio-polymer after cellulose.[41] Besides the technical advantage of the lignin-based raw materials for anode generation, extracting this material is also not difficult. By applying an

[a]Institute of Theoretical Chemistry, Ulm University, D-89081 Ulm, Germany. E-mail: jafar-1.azizi-shoushbolaghi@uni-ulm.de; axel.gross@uni-ulm.de
[b]Institute of Physical and Theoretical Chemistry, Tübingen University, 72076 Tübingen, Germany. E-mail: holger.euchner@uni-tuebingen.de

aqueous alkaline solution to the fibers, lignin can be gradually and selectively extracted.[40]

Lignin-derived carbon fibers (LCFs) have already been incorporated in LIB anodes because of the materials' intriguing qualities.[42,43] According to recent studies, lignin can be a domestic and sustainable source of nanostructured hard carbons with broad potential for use in energy storage.[44,45] With its amorphous, cross-linked three-dimensional structure, lignin is a very prominent, abundant, and renewable resource. Lignin can be pyrolyzed and reduced to create carbon–carbon composites made of crystalline (graphitic) and amorphous domains, according to processing–structure–property–performance (PSPP) research.[46,47] The selection of lignin feedstock, processing, and carbonization temperature can be used to adjust the volume fraction, porosity, and geometry of lignin-derived hard carbons.[48,49] While the porosity and pore size[50,51] can be highly affected by the feedstock, at higher pyrolysis temperatures, the volume of closed pores in the hard carbon increases.[52] Hence, understanding and controlling the process parameters allows for tailoring the HC properties with respect to applications in Li- and post-Li-ion batteries. In this work, we investigate the creation of different HC-like structures from lignin-type precursors *via Ab Initio* Molecular Dynamics (AIMD) simulations. Lignin-based compounds like $H_{88}C_{80}O_{24}$ (5,5′-diacetyl-2,2′,3,3′-tetramethoxybiphenyl) are commodity chemicals that are used as intermediates in the production of numerous significant industrial goods, including acids. The primary method employed to elucidate the complex lignin structure was the synthesis from simple molecule-based structures. The reliability of this process has been assessed by NMR and IR analyses of the lignin structure and comparison to the generated model compounds.[53,54] Here, we follow the same approach and consider rather simple model structures, while more complex phases may be produced from similar structural units. This approach most likely does not fully uncover the HC structure but provides valuable insight into porosity and pore size as well as defects and impurities, and the resulting presence of undercoordinated active sites. Furthermore, the impact of preparation temperature, underlying polymer type, and different impurities on the generated HC is taken into account. HC prepared from different raw materials and under different preparation conditions transforms into different types of structures, strongly affecting the available AM storage capacity and the storage mechanism, and hence the suitability for battery applications. After generating model systems with different HC morphologies, to evaluate the structural stability during AM storage, AM-atom intercalation energies and resulting charge/discharge curves were determined. The structures allow for the uptake of increased AM concentrations without significant structural distortion. While the HC morphology results in a largely increased capacity as compared to pristine graphite, the loss of active material during the charge/discharge process, due to strong bonding at defect sites, is inevitable, but can, however, at least be partially reduced by hydrogen saturation. This theoretical study can offer helpful details on the interaction mechanisms in lignin-derived HC and yield insights that may be used to increase the capacity of carbon derivatives for anode applications.

2 Computational methods

To investigate the impact of temperature on the geometry of lignin-derived HC materials, different lignin-based polymer structures were considered. In particular, phases with $H_{88}C_{80}O_{24}$ (~20.1 × 15.4 × 7.1 Å),[53] $H_{64}C_{128}$ (~11.5 × 12.9 × 14.8 Å),[55] $X_{104}C_{428}$ (~48.5 × 21.7 × 10.7 Å, with X = C, O, S) and $N_{56}C_{428}$ (~45.1 × 21.0 × 10.2 Å) stoichiometry, hereafter referred to as lignin-α, lignin-β, X-lignin-γ and N-lignin-γ have been investigated (see Fig. 1, and S1 in the SI). The lignin-α, β, and γ model systems were constructed to represent key structural motifs derived from the dominant interunit linkages in lignin, which largely determine the three-dimensional architecture of the biopolymer. These models span systematic variations in heteroatom content, crosslinking density, and aromatic connectivity that arise during lignin depolymerization and carbonization. More specifically, the lignin-α model represents relatively small, less aromatized structures with a higher fraction of functional groups, mimicking early-stage pyrolysis intermediates. In contrast, the lignin-β model contains a higher fraction of aromatic rings and a more crosslinked network, reflecting more aromatized structures with fewer dangling bonds. The lignin-γ models (including heteroatom-containing variants such as N-, O-, and S-lignin-γ) represent larger, more extended systems with increased structural complexity,

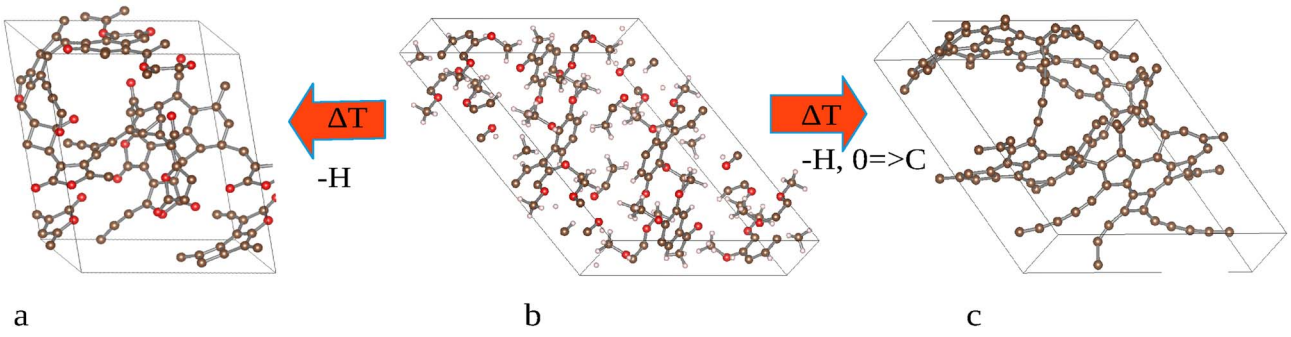

Fig. 1 Schematic depiction of the structure preparation at 1273 K: the (a) oxygen-containing O-lignin-α model system (with hydrogen being removed), (b) raw material, and (c) C-lignin-α model system (with hydrogen being removed and oxygen replaced by carbon).

containing a higher fraction of dangling bonds and active sites compared to both previously mentioned models, and fewer aromatic rings, thereby capturing the influence of feedstock variability and heteroatom incorporation.

Furthermore, structures created from C_{300} (~28.0 × 26.0 × 8.0 Å), C_{240} (~26.0 × 26.0 × 8.0 Å) and C_{240} (~26.0 × 26.0 × 8.0 Å) nano-ribbons, referred to as NR-I, NR-II and NR-III, were studied. It has to be noted that the initial conditions for NR-II and NR-III differed with respect to the arrangement of the nanoribbons (for further structural details see Fig. 2 as well as Fig. S1 and S2 in the SI). These nanoribbon based model structures were introduced as limiting cases with pre-organized graphitic domains, allowing the assessment of the impact of initial structural ordering. Rather than reproducing exact molecular structures, these models are designed to sample a representative range of local environments characteristic of lignin-derived hard carbons and to enable a systematic investigation of structure–property relationships.

The aforementioned structures were extracted during AIMD simulations performed in the canonical ensemble at temperatures of 1273 K, 1573 K, and 1773 K. This temperature range is representative of experimental pyrolysis conditions and facilitates sufficient bond rearrangements within the limited timescales accessible to the simulations.[56–60] Each simulation was run for more than 40 ps with a time step of 1 fs using the Nosé–Hoover thermostat, which is sufficient to generate disordered carbon structures with characteristic features such as bond reorganization and pore formation. It should be noted that the present approach is not intended to reproduce the full experimental pyrolysis process, which occurs on much longer timescales, but rather to generate representative metastable structures for further analysis. In this context, the use of simplified atomistic model systems, as employed here and in previous studies,[61,62] allows for the systematic investigation of key structural motifs such as heteroatom content, crosslinking, and local coordination environments. While this approach does not capture the full macromolecular complexity of lignin-derived hard carbons, it provides meaningful insight into local structural transformations and AM–carbon interactions. Similar AIMD-based approaches have been widely applied to study disordered carbon systems and have been shown to capture essential features such as bond breaking, structural rearrangement, and pore formation on short timescales.[56–60] The structural characteristics obtained in this work, including disordered carbon networks and intrinsic void regions, are consistent with experimentally observed features of lignin-derived and other hard carbon materials.[63–67] Therefore, despite the inherent limitations related to system size, timescale, and chemical complexity, the present approach provides a physically meaningful basis for establishing qualitative structure–property relationships.

The AIMD simulations in this work were performed at the temperatures mentioned above, which are representative of experimental carbonization conditions for lignin-derived hard carbons. While lower temperatures are relevant to earlier stages of pyrolysis, structural evolution at such temperatures occurs on significantly longer timescales that are not accessible within AIMD simulations. As a result, simulations at lower temperatures would not lead to substantial bond rearrangements or pore formation within the accessible simulation time (tens of picoseconds). The chosen temperature range therefore enables the observation of relevant structural transformations within computationally feasible timescales, while remaining consistent with experimentally applied carbonization conditions. Consequently, the generated structures should be interpreted as representative configurations of thermally treated carbon materials, rather than a detailed description of the full pyrolysis pathway at low to high temperature. Subsequently, the extracted structures were fully optimized with respect to the lattice parameter and atomic positions. The relatively small simulation cell size restricts the description of long-range structural features such as pore connectivity and size distribution; therefore, the present results should be interpreted primarily in terms of local bonding environments and short-range structural characteristics. The different lignin type structures as well as the nanoribbon-based structures, were then investigated with respect to geometry, stability, porosity formation, and impact of initial conditions (*e.g.*, the orientation of the ribbons in the unit cell, see Fig. S1e and f in the SI). Furthermore, structures derived from lignin-α and lignin-β were analyzed and investigated for AM insertion. All simulations were performed with the Vienna *Ab Initio* Simulation Package (VASP),[68] using the Projector Augmented Wave (PAW) approach,[69] which is well-suited to study properties of battery materials from first principles.[70] Exchange and correlation were described *via* the optPBE functional, which includes a non-local correction scheme to account for van der Waals interactions.[71] Atomic structures were optimized until the ionic geometry converged to force differences below 10^{-2} eV Å^{-1} and the electronic self-consistent field (SCF) energy difference dropped below 10^{-5} eV. Each structure was optimized with respect to the lattice constant and atomic positions, applying a plane wave cutoff of

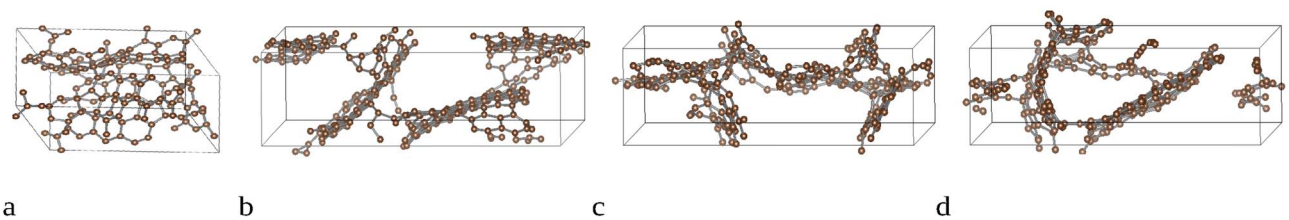

Fig. 2 Model structures derived at 1273 K, from (a) lignin-β and (b–d) different types/sizes of the nano-ribbons (for more information see Fig. S1 and S2 in the SI).

600 eV and using a *K*-point resolution of ≈ 0.2 Å^{-1}, while the plane wave cutoff and *K*-point resolution for the AIMD calculations were set to 400 eV and ≈0.5 Å^{-1}, respectively.

3 Results and discussion

3.1 Lignin based polymers

The investigation of different model structures, obtained from the above-introduced types of polymers/nanoribbons, shows that the resulting morphologies are significantly affected by the preparation conditions, yielding different pore sizes and density distributions.

First, snapshots from AIMD runs of the lignin-α structure at temperatures of 1273 K, 1573 K, and 1773 K were extracted (see Fig. 1). Experimentally, such high temperatures result in the evaporation of hydrogen and even oxygen. We, therefore, considered several different scenarios. In the first one, all hydrogen atoms were removed (O-lignin-α, see Fig. 1), while in the second one, the pyrolysis process was mimicked by additionally replacing all oxygen atoms with carbon (C-lignin-α). Finally, hydrogen was added to C-lignin-α and O-lignin-α, resulting in a saturation of dangling bonds and structures which, hereafter, will be referred to as HC-lignin-α and HO-lignin-α (see Fig. 3a and b). Hydrogen passivation was employed as a computational strategy to eliminate artificial dangling-bond states and stabilize the electronic structure.[72,73] However, this treatment represents an idealized approximation and does not fully capture the chemical complexity of real lignin-derived carbon materials. In this context, hydrogen passivation can be viewed as a simplified model for the passivation effects arising from residual hydrogen or functional groups present in experimentally derived carbons. For the cases of lignin-β-, lignin-γ-, and NR-derived structures, the same preparation routine was followed. The increased temperatures of the AIMD simulations (between 1273 K and 1773 K) result in the formation of semi-graphitic domains which are interconnected by sp^3 hybridization, yielding amorphous-like and highly disordered structures. The number of such semi-graphitic domains, consisting of joint hexagonal units, increases with higher temperatures, also meaning a decreasing number of dangling bonds. To better quantify the morphological differences of the obtained structures, their respective porosity was calculated *via* the following expression:[74]

$$\text{Porosity}\ (\%) = \left(V_{\text{sys}} - V_{\text{gra}}\right)/\left(V_{\text{sys}}\right) \times 100 \quad (1)$$

where V_{sys} represents the volume of the model system and V_{gra} corresponds to the volume of graphite with an equal number of carbon atoms. It should be noted that the porosity metric employed here represents a relative measure of excess volume compared to graphite. While it enables meaningful trend comparisons across model systems, it does not necessarily describe the experimentally accessible porosity, which depends on pore size distribution, connectivity, and ion accessibility. In the case of C-lignin-α, increasing the temperature from 1273 K to 1573 K results in an increase in porosity from 34% to 47%, followed by a strong decrease to 30% at a temperature of 1773 K (see Fig. 3c and Table 1). These differences in porosity are expected to strongly affect the respective AM storage capacity, which will be addressed further below.

Next, the above-introduced O-lignin-α type structures, which still contain oxygen while hydrogen was removed, were investigated. As in the previous scenario, the temperature was increased from 1273 K to 1773 K. Again, this results in more semi-graphitic domains and significantly decreases porosity for the high temperature structure (even more pronounced than before; see Fig. S3 in the SI). Here, it has to be noted that a small fraction of the carbon and oxygen atoms formed carbon monoxide (CO) molecules, which were then removed from the

Table 1 Porosity for C-lignin-α, O-lignin-α, and C-lignin-β at different temperatures (for further information about the other model systems' porosity see Table S1 in the SI). It should be noted that the number of H atoms after model saturation is not considered in eqn (2)

Δ*T*	1273 K	1573 K	1773 K
C-lignin-α	34%	47%	30%
HC-lignin-α	31%	42%	31%
O-lignin-α	33%	42%	19%
HO-lignin-α	34%	42%	21%
C-lignin-β	40%	14%	12%
HC-lignin-β	38%	17%	17%

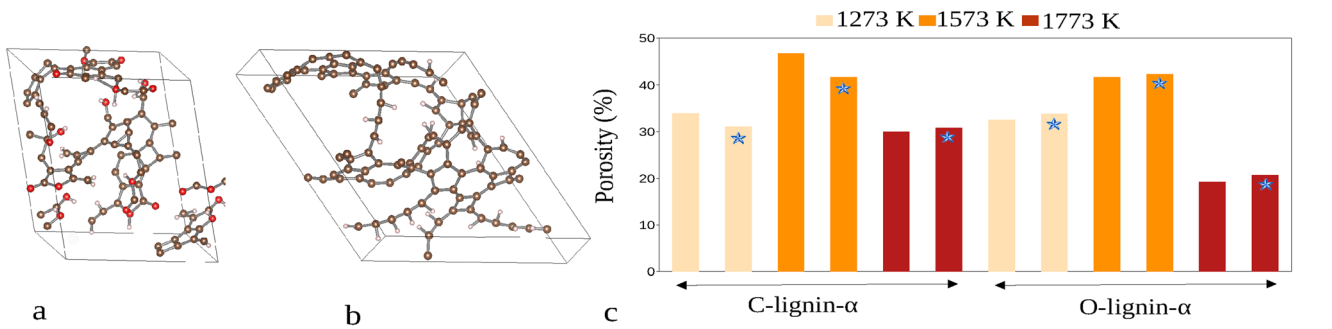

Fig. 3 (a and b) Hydrogen saturation of the lignin-α model system that was prepared at 1273 K (O-lignin-α and C-lignin-α, see Fig. 1); (c) porosity of the lignin-α derived model system at different temperatures (1273 K, 1573 K, and 1773 K). The star sign shows hydrogen-saturated model systems.

system. Due to the CO formation and removal, the final structures obtained at different temperatures show slightly varying stoichiometries corresponding to $C_{71}O_{15}$ (O-lignin-α (1273 K)), $C_{76}O_{20}$ (O-lignin-α (1573 K)) and $C_{69}O_{13}$ (O-lignin-α (1773 K)). For the 1273 K structure, the porosity of O-lignin-α amounts to ≈ 33%, showing almost the same porosity as C-lignin-α obtained at this temperature. The high temperature structures (1773 K), on the other hand, differ strongly, with O-lignin-α demonstrating a significantly reduced porosity of 19%, which is much lower than the 30% of the corresponding C-lignin-α. Furthermore, for both model systems, the maximum porosity is obtained at 1573 K, while increasing or decreasing the temperature leads to a decrease in the porosity (see Fig. 3c). For the C-lignin-β model system, the scenario is somewhat different. While the maximum porosity (≈40%) is obtained at a temperature of 1273 K, increasing the temperature results in a highly decreasing porosity of ≈ 14% and ≈ 12% at 1573 K and 1773 K. This finding shows that raw materials, with an increasing fraction of carbon rings, drastically reduce the number of undercoordinated atoms in the final structure. On the other hand, the system becomes more temperature-sensitive; in other words, when the temperature increases, the model system transitions toward a layered structure, resulting in a significant reduction in both porosity and the interlayer distance. (see Fig. S4 in the SI). Finally, HC-lignin-α, HO-lignin-α, and HC-lignin-β are considered, showing a negligible porosity variation as compared to C-lignin-α, O-lignin-α, and C-lignin-β (see Fig. 3). The hydrogen saturated model systems obtained from C-lignin-α at 1273 K, 1573 K, and 1773 K exhibit a $C_{104}H_{26}$ stoichiometry and show a slight porosity change from ≈ 34% to ≈ 31%, from 47% to 42%, and from 30% to 31%, respectively. HO-lignin-α, corresponding to $O_{15}C_{71}H_{18}$ (1273 K), $O_{20}C_{76}H_{20}$ (1573 K), and $O_{13}C_{69}H_{12}$ (1773 K) stoichiometry, shows a negligible porosity change from ≈ 33% to ≈ 34% at 1273 K, and from 19% to 21% at 1773 K, while it remains at ≈ 42% for the 1573 K structure. Finally, HC-lignin-β, corresponding to the $H_{11}C_{128}$ model system, also shows a negligible variation in porosity as compared to the C-lignin-β model systems. For the model systems created at 1273 K, 1573 K, and 1773 K the porosity after hydrogen saturation changes from 40%, 14% and 12% to 38%, 17%, and 17%, respectively (see Tables 1 and S1 and Fig. S4 and S5 in the SI).

In general, the porosity exhibits a non-monotonic dependence on temperature, increasing from 1273 K to 1573 K and subsequently decreasing at 1773 K. The initial increase in porosity can be attributed to enhanced bond rearrangement and the formation of void regions at intermediate temperatures. At higher temperatures, however, structural densification and partial collapse or coalescence of pores may occur, leading to a reduction in overall porosity. This evolution in pore structure has important implications for ion storage behavior: while increased porosity at intermediate temperatures facilitates the AM accommodation within the carbon matrix, excessive structural reorganization at higher temperatures may reduce the availability of accessible storage sites. This observation highlights the existence of an optimal structural regime for maximizing the AM uptake.[75,76]

3.2 Feedstock impact on model systems

From the above-presented results for the lignin-α and C-lignin-β based structures, it becomes evident that the morphology of the precursor material, characterized by polymer size and type, strongly affects the geometry and porosity of the respective model system. A very small polymer, for instance, with fewer hexagon rings produces a more amorphous-like structure with more unsaturated bonds. A larger polymer, on the other hand, with more hexagons rather than merely carbon chains, reduces the amount of unsaturated bonds and increases the porosity, as shown in the case of C-lignin-β. In the following section, the impact of the raw material on the resulting HC structure is further examined for the cases of the C-lignin-γ, N-lignin-γ, O-lignin-γ, S-lignin-γ, and for the model systems generated from the nano-ribbons (see Fig. 2 and also Fig. S1 and S2 in the SI). In this paragraph, the discussion is limited to structures created at 1273 K. The porosity for the C-lignin-γ, S-lignin-γ, N-lignin-γ, and O-lignin-γ structures amounts to 52%, 50%, 44%, and 43%, respectively. These values show an increased porosity as compared to previously discussed model systems like lignin-α, and lignin-β (see Table S1, and Fig. S1 and S2 in the SI). While the polymer size in these model systems is larger (a large chain of polymers), the final structure shows higher porosity (see Fig. S1 in the SI). However, the obtained structures show an increased number of unsaturated/dangling bonds, which is one of the issues that needs to be solved for using them as an anode material. Strong bonding of the AM atoms to these uncoordinated sites makes them rather unsuited for battery applications[77,78] To further evaluate the effect of the raw material, we also considered the evolution of the nanoribbon-based structures. The different nano-ribbon derived models show varying porosity, which originates from their initial structural characteristics, such as the hexagon ratio, chain length, and orientation of the nanoribbons (see Fig. 2). With a value of 53%, NR-I shows the highest porosity, followed by NR-II with 44%. For NR-I and NR-II, the final structures – unlike the usual model structures from polymers (chain/less-hexagon-rings) which are full of unsaturated bonds – show large graphitic domains and consequently a more pronounced porosity. For NR-III, a porosity of 32% is observed, which shows that the initial condition can highly affect the final model structure.

3.3 AM-insertion

As a next step, AM insertion at different sites of the C-lignin-α, O-lignin-α, and C-lignin-β model systems was investigated (see Tables 2, 3, and S2 in the SI). For the C-lignin-α and O-lignin-α systems, the energetically most favorable AM adsorption sites were determined for the structures created at temperatures of 1273 K, 1573 K and 1773 K (see Fig. 4). Different insertion sites were investigated, anticipating that the presence of unsaturated bonds will make the AM adsorption highly favorable.[79] For the C-lignin-α structure, prepared at 1273 K (see Fig. 5a–c), AM atoms placed at several different positions were found to move to undercoordinated sites, showing that unsaturated bonds are more favorable for AM atoms than the large porous sites. The preferential adsorption of alkali metals at undercoordinated

Table 2 Insertion energy E_{int} (in eV) for Li, Na, and K atoms in different sites of C-lignin-α and C-lignin-β prepared at a temperature of 1273 K (see Fig. 5, and S6 and S9 in the SI)

Sites	$N = 1$	$N = 2$	$N = 3$	$N = 4$	$N = 5$
LiC-lignin-α	−1.32	−1.92	−1.97	−1.33	−1.71
NaC-lignin-α	−2.00	−1.82	−1.58	−1.74	—
KC-lignin-α	−2.53	−1.88	−2.33	−2.41	—
LiHC-lignin-α	−0.98	−1.10	−1.10	−0.83	—
NaHC-lignin-α	−0.89	−1.82	−0.69	−0.70	−0.27
KHC-lignin-α	−1.93	−1.96	−1.7	−1.60	−1.32
LiC-lignin-β	−1.12	−1.81	−1.62	−1.27	−1.0
NaC-lignin-β	−1.16	−1.84	−1.60	−1.1	−1.1
KC-lignin-β	−1.94	−2.22	−2.27	−1.87	−1.83
LiHC-lignin-β	−1.0	−0.82	−0.81	−1.0	−1.0
NaHC-lignin-β	−0.26	−1.1	−1.1	−1.1	−0.9
KHC-lignin-β	−1.32	−1.53	−1.45	−1.76	−1.17

Table 3 Insertion energy E_{int} (in eV) for Li, Na, and K atoms in different sites of C-lignin-α prepared at temperatures of 1573 K and 1773 K (see Fig. S8 in the SI)

Sites	$N = 1$	$N = 2$	$N = 3$	$N = 4$	$N = 5$
$Li_{\Delta T1573}$	−0.58	−1.25	−1.49	−1.21	−1.73
$Na_{\Delta T1573}$	−2.14	−1.60	−1.34	−1.56	—
$K_{\Delta T1573}$	−2.58	−2.31	−2.30	—	—
$Li_{\Delta T1773}$	−2.48	−1.38	−1.14	−1.19	—
$Na_{\Delta T1773}$	−1.48	−2.50	−1.43	−1.24	—
$K_{\Delta T1773}$	−2.19	−2.89	−2.22	−2.94	—

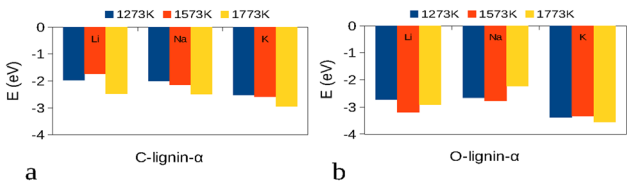

Fig. 4 The most favorable sites for insertion of a single AM atom regarding (a) C-lignin-α and (b) O-lignin-α.

carbon sites is thermodynamically expected and may also be responsible for the irreversible capacity due to possible ion trapping at defect sites.[80,81] Furthermore, increasing the AM content results in an up-shift of the Fermi energy (see Fig. 6), which is more pronounced for Na and K as compared to the case of Li. These differences in the Fermi level up-shift also indicate that Na and K affect the geometry of the structure more severely than Li.[82,83] Hydrogen saturation of the HC-lignin-α (1273 K) structure results in decreased adsorption strength and corresponding insertion energies of −1.1 eV, −1.98 eV, and −1.96 eV for Li, Na, and K at the most favorable sites. Finally, an investigation of the samples that were prepared at 1573 K and 1773 K (see Fig. S8 in the SI) again shows that all AM-atoms move towards unsaturated bonds. The most stable adsorption sites are observed for the high temperature model (1773 K), amounting to −2.48 eV, −2.50 eV, and −2.94 eV for Li, Na, and K, respectively (see Fig. 4a).

For the O-lignin-α (1273 K) model system not only unsaturated carbon bonds but also sites close to the oxygen atoms are energetically highly favorable for AM ion adsorption (see Fig. 4b, and S8, and S9 in the SI). As for the case of C-lignin-α, the AM atoms placed at different initial positions move to unsaturated bond sites. The most favorable adsorption sites of this system show significantly increased adsorption strength as compared to C-lignin-α (1273 K), yielding energies of 2.72 eV, −2.65 eV, and −3.38 eV for Li, Na, and K, respectively. Similar to the case of HC-lignin-α (1273 K), the hydrogen saturated HO-lignin-α (1273 K) shows less strong adsorption, with the corresponding insertion energies for the most favorable sites amounting to −1.54 eV (Li), −1.1 eV (Na), and −2.86 eV (K) (see Table S3 in the SI). Hence, the hydrogen saturation more strongly alters the insertion energy for O-lignin-α as compared to the C-lignin-α structure, which is due to the saturation of highly active sites, created in the presence of oxygen. Interestingly, for the O-lignin-α model system, the strongest adsorption for Na and Li is observed for the 1573 K structure. The energies of the most favorable sites in this system – corresponding to −3.19 eV, −3.15 eV, and −3.33 eV for Li, Na, and K – are shown in Fig. 4b. In the case of the 1773 K O-lignin-α structure, the most favorable sites show less strong adsorption for Li (−2.91 eV) and Na (−2.23 eV) while the K adsorption strength is increased to −3.55 eV. For this model system, the porosity is highly reduced, and the porosity-size/graphite-layer-distance (≈4 Å) significantly decreases in some points, such as the heptagon site. Hence, the AM atoms that are inserted at this site – which also lacks oxygen – show less favorable insertion energies (for Li (−0.73 eV), Na (−0.54 eV), and K (−0.60 eV)) in comparison to the other sites and model systems. A close look at the model system shows that the charge distribution is different for oxygen-containing and oxygen-free structures, as can be inferred from the corresponding charge density difference plots (see Fig. 7).

The latter ones reveal pronounced charge accumulation around undercoordinated carbon atoms and within local void regions, indicating that these sites act as energetically favorable adsorption centers for AM atoms. This redistribution of electron density suggests a strong interaction between the AMs and defect-rich regions of the carbon framework, which contributes to enhanced storage capacity. Indeed, the charge transfer from the AM atoms to the oxygen-containing carbon framework is extended to the oxygen sites. This indicates that the bonding of AM atoms to this system will be stronger than for the oxygen-free system, which is in agreement with the observed adsorption energies. To generalize this finding, the most favorable sites in the C-lignin-α and O-lignin-α model system were considered. Charge analysis of the C- and O-lignin-α structures, using the DDEC6 charge analysis scheme, yields a charge transfer of 0.70 e, 0.77 e, 0.83 e, and 0.84 e, 0.88 e, 0.90 e for Li, Na, and K, respectively. This points to a higher reactivity of the oxygen sites, which is the reason for the stronger AM adsorption in the O-lignin-α system (see Fig. 7).

Finally, AM atoms positioned at various sites for the C-lignin-β structure, which was produced at 1273 K (see Fig. S6 in the SI), were considered. As for the case of C-lignin-α and O-lignin-α,

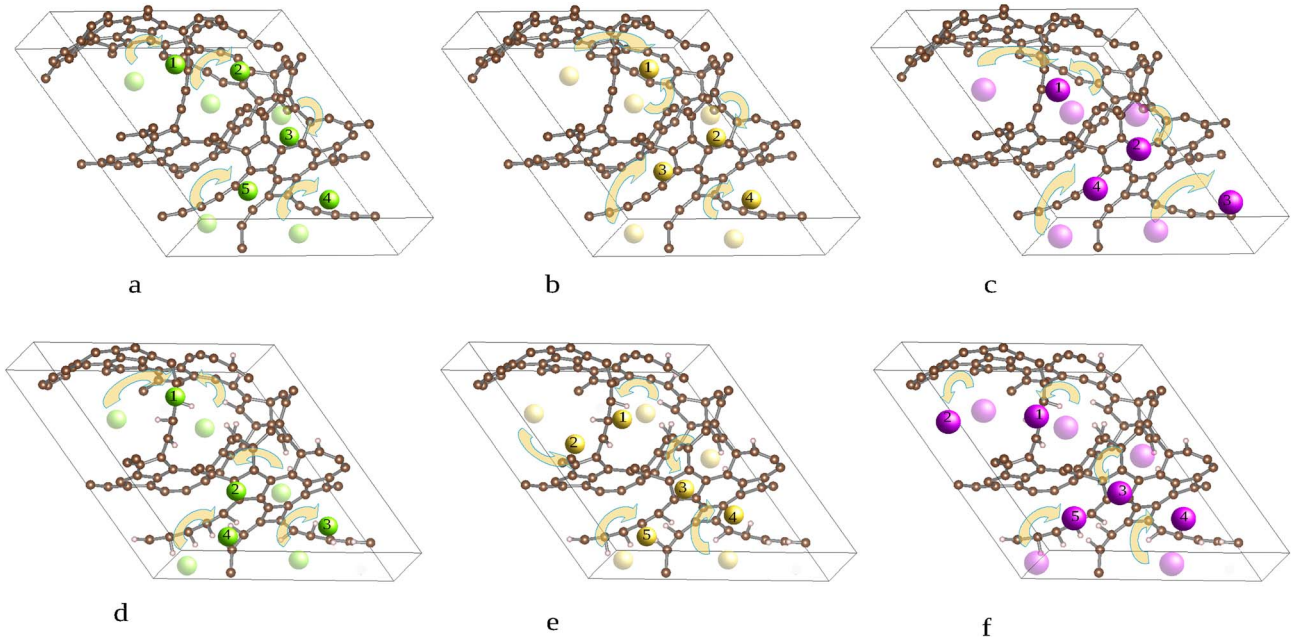

Fig. 5 Schematic representation of the Li (green), Na (yellow), and K (purple) insertion (a–c) for C-lignin-α and (d–f) for HC-lignin-α. The model structures are created at a temperature of 1273 K (for more information about the other models, see Fig. S6 in the SI).

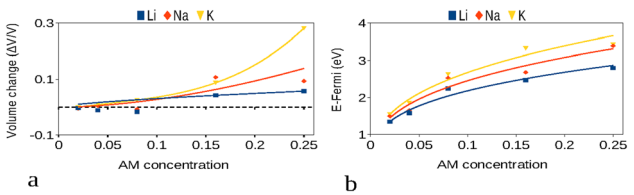

Fig. 6 (a) Volume change and (b) Fermi energy shift of the C-lignin-α model system with respect to the AM concentration. For more information, see Fig. S9 in the SI.

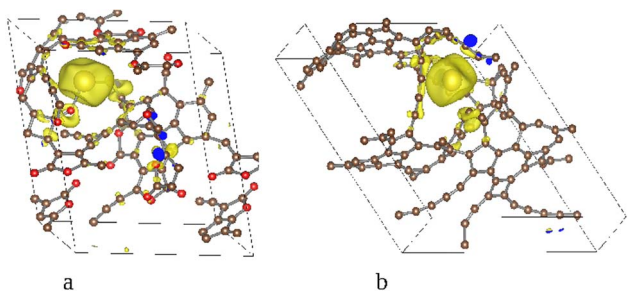

Fig. 7 Charge density differences for Na adsorption on the (a) O-lignin-α and (b) C-lignin-α model system.

the inserted atoms were observed to migrate to under-coordinated sites, again indicating that AM atoms prefer unsaturated bonds over large porosity sites. For the most favorable sites the insertion energy for Li, Na, and K in C-lignin-β amounts to −1.81 eV, −1.84 eV, and −2.27 eV, respectively. These energies are 0.16 eV (Li), 0.16 eV (Na), and 0.26 eV (K) less negative as in the case of C-lignin-α, whereas in comparison to O-lignin-α the differences amount to 0.9 eV, 0.8 eV, and 1.1 eV for Li, Na, and K, respectively. Here, a DDEC6 based charge analysis yields a charge transfer of 0.67 e, 0.74 e, and 0.75 e, for Li, Na, and K, respectively. This means a reduced charge transfer as compared to the previously discussed cases (C-lignin-α and O-lignin-α), confirming the lower reactivity of the C-lignin-β structure. The hydrogen saturation of this system (HC-lignin-β) reveals that the insertion energy at the most favorable sites for Li, Na, and K is altered to −1.0 eV, −1.2 eV, and −1.76 eV, respectively. Hence, hydrogen saturation strongly alters the insertion energy and reduced the adsorption strength in C-lignin-β, as well as in the lignin-α model systems.

Insertion compounds with higher AM content have also been studied, to allow for the determination of the resulting open circuit voltage (OCV). For this purpose, AIMD simulations at 400 K were performed to distribute different numbers of AM atoms in the respective model system. First, the carbon matrix was kept fixed while the AM atoms were free to move (more than 1000 ionic steps). Afterwards, the whole structure was optimized with the C-atoms also being free to move. The resulting discharge curves have been established for a range of AMC_x stoichiometries, in order to comprehend the influence of the system geometry on the entire insertion process and the potential application as an anode material. In the following section, the AM insertion for model systems created at 1273 K is investigated. The reason for focusing on these systems is the fact that this temperature corresponds to the beginning of the HC formation under experimental conditions.[84] An increasing number of AMs was inserted in the respective structures, and the corresponding charge/discharge curves were determined (see Fig. 8, 9, and also Fig. S7 in the SI). The following formula

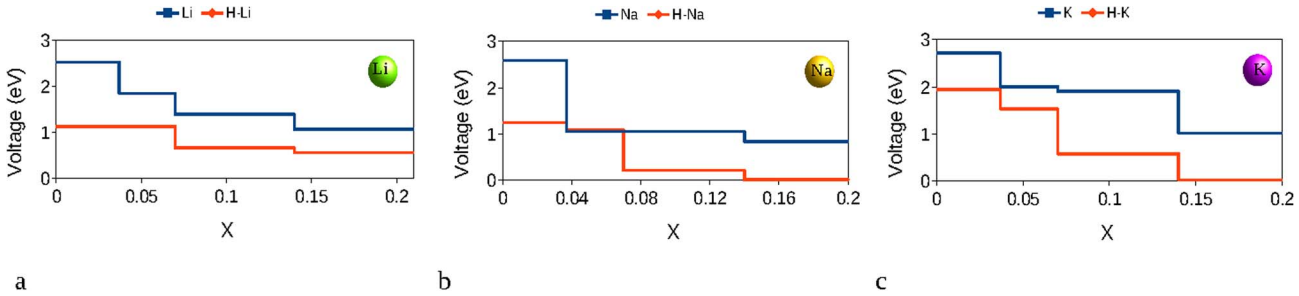

Fig. 8 Discharge curves for the insertion of (a) Li, (b) Na, and (c) K in the lignin-derived (C-lignin-α) polymer model structure. Voltage curves are only shown for the structure that was created at 1273 K (see Fig. 1c). X denotes the concentration of inserted atoms in the investigated model systems (X corresponds to the number of inserted AM atoms divided by the total number of atoms). H-AM shows the AM concentration in a hydrogen-saturated mode system, HC-lignin-α.

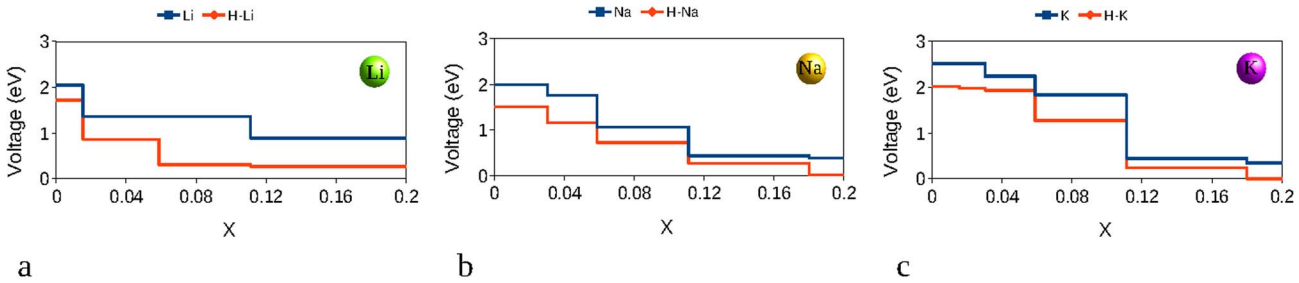

Fig. 9 Discharge curves for C-lignin-β (1273 K), for (a) Li, (b) Na, and (c) K insertion. X denotes the concentration of inserted atoms in the investigated model systems (X corresponds to the number of inserted AM atoms divided by the total number of atoms). H-AM shows the AM concentration in a hydrogen-saturated model system, HC-lignin-β.

has been used to calculate the open circuit voltages (OCV) of the most stable configurations at a given AM concentration in relation to the respective bulk metal.

$$V_{\mathrm{OCV}} = (E_{x+1} - (E_x + E_{\mathrm{AM}}))/z \quad (2)$$

where x is the ion content and z corresponds to the elementary charges that are transferred during the insertion process. E_{AM} represents the energy of the bulk metal phase.

The AM atom insertion shows that the considered model systems not only improve the capacity for Li and K ions beyond that of graphite (the highest concentrations that can be realized for Li and K in graphite correspond to LiC_6 and KC_8), but a largely increased capacity is also observed for Na storage. Regarding C-lignin-α and C-lignin-β, AM storage is possible up to AMC_4 stoichiometry and even beyond (see Fig. S10 in the SI). However, due to the higher density of defects and unsaturated bonds, the adsorption energy of the AM atoms, in particular at lower AM concentrations, is strongly negative, which results in potentials of above 1.0 V for Li, Na and K storage in both model systems (for $x \leq 0.14$), as can be inferred from Fig. 8 and 9. When, instead, hydrogen saturated structures are considered,[85,86] the AM insertion energies at low concentration are found to be strongly altered by up to 1.0 eV, for all considered model systems (see Table 2), thus significantly lowering the corresponding potential (see Fig. 8). A comparison of HC-lignin-α and C-lignin-α shows that the hydrogen saturation lowers the insertion energy and consequently shifts the potentials below 1.0 V for Li, Na and K storage in HC-lignin-α (for $x \geq 0.07$) as depicted in Fig. 8. Similarly, AM insertion in the high porosity HC-lignin-β phase, obtained at 1273 K, shows that the insertion energy becomes less negative, resulting in a smaller voltage at low AM concentration, as compared to the plain C-lignin-β phase (by ≈ 0.3 eV, ≈ 0.5 eV, and ≈ 0.5 eV for Li, Na, and K, respectively, see Fig. 9). Moreover, the O-lignin-α structure was also considered for OCV calculations, again showing rather increased voltages which can be expected to be lowered by hydrogen saturation (see Fig. S7 in the SI).

Besides hydrogen saturation, which highly alters the insertion energy, the initial morphology of the raw material also plays an important role in the resulting potential profile. As already mentioned, polymers with more hexagonal units result in final structures with larger porosity and fewer unsaturated bonds, as discussed for the comparison of 1273 K structures of lignin-β and lignin-α.

Comparing HC-lignin-α and HC-lignin-β shows that hydrogen saturation affects the voltage profile of C-lignin-α more significantly. The reason behind this might be the larger amount of uncoordinated bonds in C-lignin-α, which results in an increased initial insertion energy and consequently OCV, which is strongly altered after hydrogen saturation. In general, it has to be pointed out that the calculated voltage profiles provide a semi-quantitative description of alkali-ion storage behavior, capturing relative trends and structural dependencies while not aiming for exact quantitative agreement with

experiments. Nevertheless, this approach allows us to identify how variations in porosity, disorder, and local bonding environments, including hydrogen saturation, influence the shape and features of the voltage profile.

In previous reports, the mechanisms of sodium storage in the slope and plateau regions of hard carbon have been explored.[87–89] The creation of a quasi-metallic sodium cluster has been reported by certain researchers, including Stratford *et al.*, using Na solid-state NMR.[90] Electron paramagnetic resonance, computation, and Raman spectroscopy have recently been used to study sodium clusters and provided insight into the sodium pore-filling process, also with respect to pore size and defect concentration. Complementary to these investigations, our calculations show that by increasing the AM concentration in the considered model systems, metallic and quasi-metallic AM clusters are formed. By considering the AM–AM distances in the C-lignin-α structure, for Li, Na, and K, minimum values in the order of 2.50 Å, 2.96 Å, and 2.90 Å are observed. These are close to the nearest neighbor distance in the respective metallic phases (see Fig. 10a–c). Moreover, for C-lignin-α and O-lignin-α the volume change under AM-insertion was considered. At low concentrations, there is no significant increase for C-lignin-α, especially for Li and Na, but increasing the intercalant concentration up to 25% (see Fig. 6) results in a considerable volume expansion of ≈6%, ≈9.5%, and ≈28.2% for Li, Na and K, respectively. The volume change during AM insertion is even higher for the oxygen-containing model system (O-lignin-α (1273 K)), which originates in the smaller initial volumes of the AM free structures. In this case, the volume change for K insertion amounts to more than 38%, while for Li and Na insertion it remains much smaller (see Fig. S9 in the SI). Furthermore, a DDEC6-based charge analysis of C-lignin-α with increased AM concentration shows that AM atoms that are adsorbed in the vicinity of uncoordinated carbon atoms transfer more than 0.8 e to the carbon framework, while for other sites (especially in large pores) a significant decrease in charge transfer is observed with ≈0.30 e, ≈0.13 e, and ≈38 e, for Li, Na, and K respectively. This indicates that the charge transfer for Na is more strongly reduced, thus pointing to a more pronounced formation of (metallic) clusters in the case of Na insertion (see Fig. 10a–c). When hydrogen saturation is considered, the AM–AM distances are not significantly changed, but the overall charge transfer is decreased. While sites with low charge transfer are observed for all AMs, the hydrogen saturated structure shows an increased number of Na atoms that can be quantified as quasi-metallic (see Fig. 11a–c).

3.4 Comparison with experimental results

To validate the relevance of the present computational results, we compare our findings with experimental studies on lignin-derived hard carbons. Such comparisons are essential to assess the physical relevance of the simplified model systems employed in this study. Experimentally, such materials exhibit disordered turbostratic structures with significant microporosity formed during pyrolysis, which plays a crucial role in the alkali metal storage behavior. Reported reversible capacities typically range between 300 and 400 mAh g^{-1}, depending on synthesis conditions and the pore structure.[91–97] In our simulations, the calculated porosity-defined here as a relative structural descriptor-ranges between approximately 30% and 50% depending on precursor type and temperature. While this metric is not directly equivalent to measured accessible pore

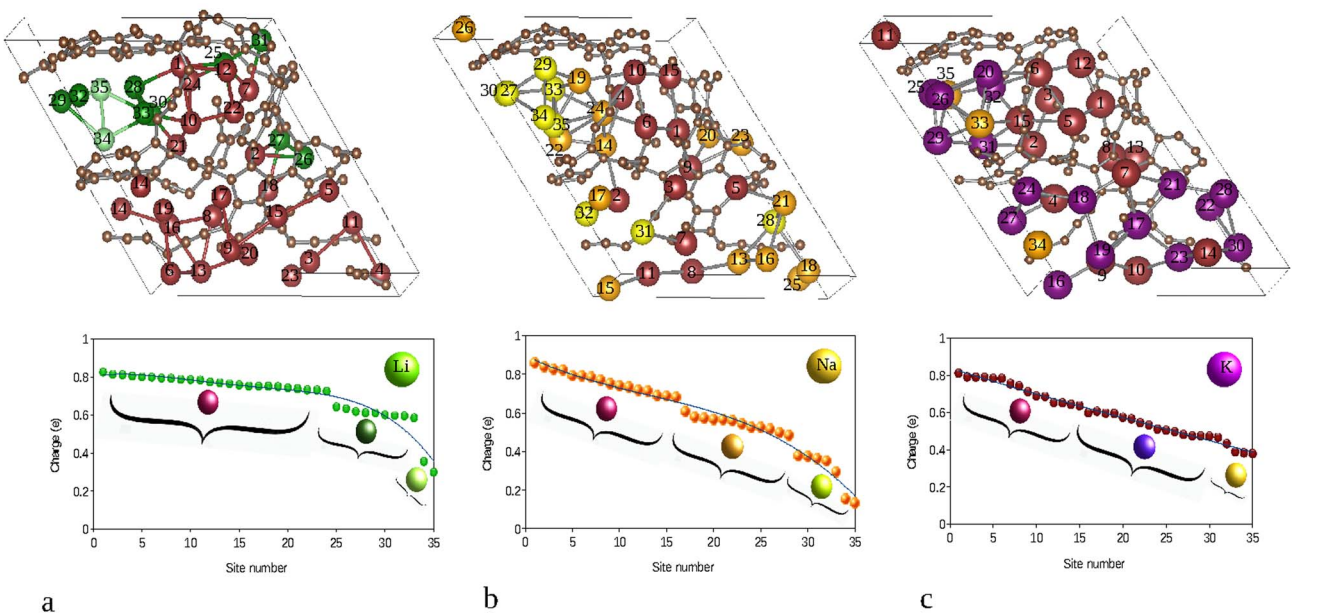

Fig. 10 Charge and bonding analysis for increased AM concentration in the C-lignin-α model system. (a–c) depict AM–AM bonds with bond distance < 3.7 Å, and charge transfer as determined from the DDEC6-charge analysis. The charge transfer (CT) for the different AMs is divided into three parts with the corresponding atoms depicted in different colors: for Li; CT > 0.60 e, 0.38 e < CT ≤ 0.60 e, and CT ≤ 0.38 e, for Na, CT > 0.64 e, 0.35 e < CT ≤ 0.64 e, and CT ≤ 0.35 e and finally for K CT > 0.6 e, 0.38 e < CT ≤ 0.6 e, and CT ≤ 0.38 e.

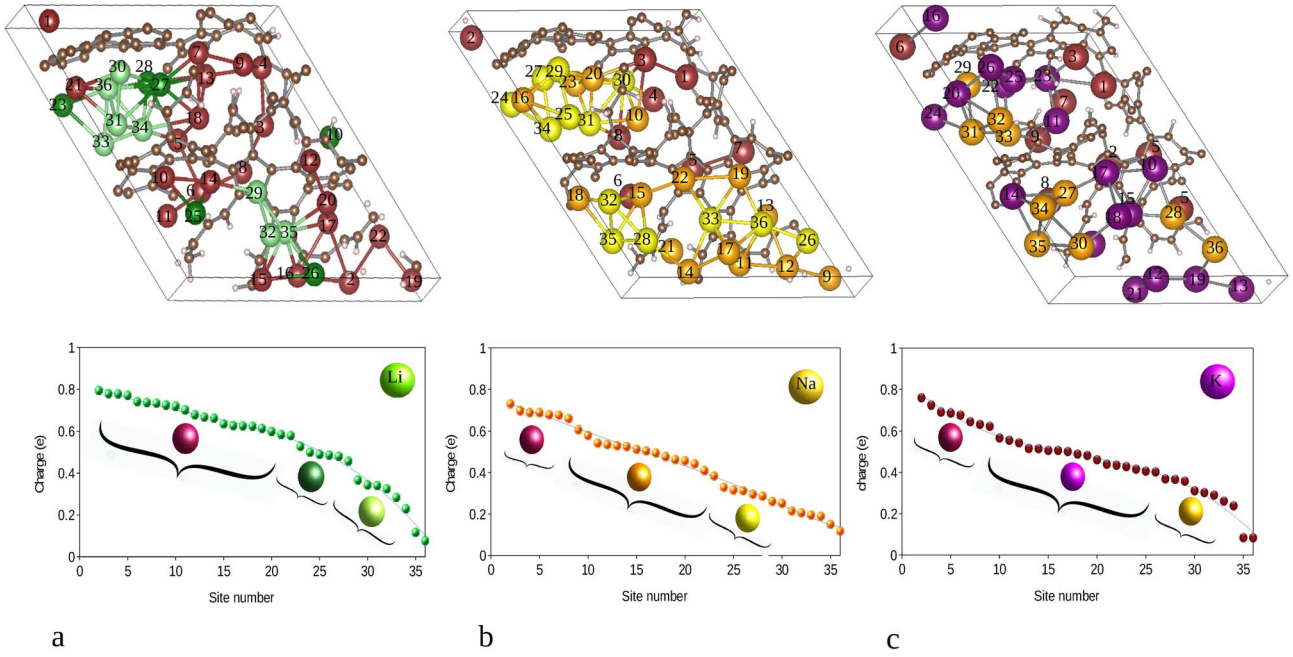

Fig. 11 Charge and bonding analysis for increased AM concentration in the HC-lignin-α model system. (a–c) depict AM–AM bonds with bond distance <3.7 Å and the charge transfer as determined from the DDEC6-charge analysis. The charge transfer (CT) for the different AMs is divided into three parts with the corresponding atoms depicted in different colors: for Li; CT > 0.52 e, 0.36 e < CT ≤ 0.52 e, and CT ≤ 0.36 e, for Na, CT > 0.60 e, 0.32 e < CT ≤ 0.60 e, and CT ≤ 0.32 e and finally for K CT > 0.56 e, 0.36 e ≤ CT < 0.56 e, and CT ≤ 0.36 e.

volumes, the observed trends are consistent with experimental findings: structures with higher porosity and increased disorder exhibit enhanced alkali metal uptake. In particular, model systems such as lignin-γ and the nanoribbon-derived structures, which show higher void fractions, also accommodate higher alkali-metal concentrations, in qualitative agreement with experimental reports linking increased pore volume to enhanced storage capacity.[98–100] It should be noted, however, that a direct quantitative comparison is limited by the simplified nature of the model systems and the definition of porosity used in this work, which does not explicitly account for pore accessibility or size distribution. Therefore, the comparison should be interpreted primarily in terms of qualitative trends, rather than absolute values. Nevertheless, the agreement between simulated structural characteristics and experimentally observed behavior supports the validity of the proposed structure–property relationships. Overall, this qualitative agreement supports the validity of the proposed structure–property relationships despite the inherent simplifications of the model systems.

5 Conclusion

Different lignin-based structures were computationally investigated with respect to their morphology and their suitability as anode materials for lithium and post-lithium-ion batteries. Structural features such as porosity as well as the AM insertion energy were studied to gain deeper insight into the properties of these materials. The created model structures are able to store significant amounts of Na and, in general, offer a largely increased storage capacity for the different AMs as compared to pristine graphite. Concerning capacity loss due to strong bonding to undercoordinated atoms in these structures, a hydrogen saturation strategy was proposed. By saturating the dangling bonds and reactive sites, insertion energies are significantly altered, and consequently, the corresponding voltage profile is shifted to lower potentials. This shift is more pronounced for C-lignin-α as compared to C-lignin-β, which is a consequence of the higher amount of uncoordinated bonds in C-lignin-α. With respect to the hard carbon morphology, we found that structures derived from lignin-γ show a higher porosity. However, due to the huge amount of undercoordinated atoms and dangling bonds, these structures are not a useful choice for battery applications. Yet, similar to HC-lignin-α, it is expected that hydrogen saturation may significantly affect the insertion energy; nevertheless, since the system mostly contains tiny pore sizes, the final structure is not expected to be a viable candidate for increased storage capacity. On the other hand, lignin-α and lignin-β, showing a highly reduced amount of uncoordinated bonds as compared to lignin-γ, may, in combination with hydrogen saturation, be suitable candidates. Our findings indicate that raw materials with an increased fraction of carbon rings increase the porosity while the number of undercoordinated atoms and dangling bonds is decreased. However, at the same time, the unsaturated carbon bonds are important for the formation of pores as opposed to graphitization, which is strongly enhanced at increased temperatures. Hence, the preparation of porous hard carbon structures from precursor materials with a fraction of carbon rings and the subsequent hydrogen saturation of

dangling bonds seems a promising strategy for creating anode materials with high capacity. Overall, our results suggest that experimental optimization should focus on (i) pyrolysis temperatures that generate disordered turbostratic carbon with well-developed but not excessive microporosity, (ii) lignin precursors with controlled heteroatom content and cross-linking to steer the resulting carbon morphology, and (iii) post-treatments (*e.g.*, gentle activation or surface functionalization) that adjust pore volume and defect density to maximize reversible alkali-ion storage while minimizing irreversible trapping.

Conflicts of interest

There are no conflicts to declare.

Data availability

Data for this article, including the density functional theory calculations, are available at the zenodo repository: https://doi.org/10.5281/zenodo.19576975.

Supplementary information (SI): additional results and figures. See DOI: https://doi.org/10.1039/d6ta00336b.

Acknowledgements

This work contributes to the research performed at Cluster of Excellence EXC 2154 "Post-Li Storage", funded by the German Research Foundation (DFG), Project ID 390874152. The authors acknowledge support from the state of Baden-Württemberg through bwHPC and the German Research Foundation (DFG) through grant no INST 40/575-1 FUGG (JUSTUS 2 cluster), the HoreKa supercomputer funded by the Ministry of Science, Research and the Arts Baden-Württemberg and the Federal Ministry of Education and Research. Furthermore, financial support by the Dr Barbara Mez-Starck Foundation is gratefully acknowledged. This work contributes to the research performed at CELEST (Center for Electrochemical Energy Storage Ulm-Karlsruhe).

References

1 M. D. Slater, D. Kim, E. Lee and C. S. Johnson, *Adv. Funct. Mater.*, 2013, **23**, 947–958.
2 C. Delmas, *Adv. Energy Mater.*, 2018, **8**, 1703137.
3 M. Wahid, D. Puthusseri, Y. Gawli, N. Sharma and S. Ogale, *ChemSusChem*, 2018, **11**, 506–526.
4 D. Shanmukaraj, K. Kretschmer, T. Sahu, W. Bao, T. Rojo, G. Wang and M. Armand, *ChemSusChem*, 2018, **11**, 3286–3291.
5 Q. Wang, C. Zhao, Y. Lu, Y. Li, Y. Zheng, Y. Qi, X. Rong, L. Jiang, X. Qi, Y. Shao, *et al.*, *Small*, 2017, **13**, 1701835.
6 Y. Kim, K.-H. Ha, S. M. Oh and K. T. Lee, *Chem. - Eur. J.*, 2014, **20**, 11980–11992.
7 T. Perveen, M. Siddiq, N. Shahzad, R. Ihsan, A. Ahmad and M. I. Shahzad, *Renew. Sustain. Energy Rev.*, 2020, **119**, 109549.
8 J. Azizi, A. Groß and H. Euchner, *ACS Appl. Mater. Interfaces*, 2025, **17**, 33965–33974.
9 H. Lei, J. Li, X. Zhang, L. Ma, Z. Ji, Z. Wang, L. Pan, S. Tan and W. Mai, *InfoMat*, 2022, **4**, e12272.
10 L. Xie, C. Tang, Z. Bi, M. Song, Y. Fan, C. Yan, X. Li, F. Su, Q. Zhang and C. Chen, *Adv. Energy Mater.*, 2021, **11**, 2101650.
11 Z. Jian, Z. Xing, C. Bommier, Z. Li and X. Ji, *Adv. Energy Mater.*, 2016, **6**, 1501874.
12 Y. Shen, J. Qian, H. Yang, F. Zhong and X. Ai, *Small*, 2020, **16**, 1907602.
13 X. Chen, Y. Zheng, W. Liu, C. Zhang, S. Li and J. Li, *Nanoscale*, 2019, **11**, 22196–22205.
14 J. Dahn, W. Xing and Y. Gao, *Carbon*, 1997, **35**, 825–830.
15 T. Zheng, Q. Zhong and J. Dahn, *J. Electrochem. Soc.*, 1995, **142**, L211.
16 D. Stevens and J. Dahn, *J. Electrochem. Soc.*, 2000, **147**, 1271.
17 M. Anji Reddy, M. Helen, A. Groß, M. Fichtner and H. Euchner, *ACS Energy Lett.*, 2018, **3**, 2851–2857.
18 H. Euchner, B. P. Vinayan, M. A. Reddy, M. Fichtner and A. Groß, *J. Mater. Chem. A*, 2020, **8**, 14205–14213.
19 K. Kubota, S. Shimadzu, N. Yabuuchi, S. Tominaka, S. Shiraishi, M. Abreu-Sepulveda, A. Manivannan, K. Gotoh, M. Fukunishi, M. Dahbi, *et al.*, *Chem. Mater.*, 2020, **32**, 2961–2977.
20 A. Tyagi, S. Puravankara, *et al.*, *Mater. Adv.*, 2022, **3**, 810–836.
21 Q. Liu, R. Xu, D. Mu, G. Tan, H. Gao, N. Li, R. Chen and F. Wu, *Carbon Energy*, 2022, **4**, 458–479.
22 H. Alptekin, H. Au, E. Olsson, J. Cottom, A. C. Jensen, T. F. Headen, Q. Cai, A. J. Drew, M. Crespo Ribadeneyra and M.-M. Titirici, *Adv. Mater. Interfaces*, 2022, **9**, 2101267.
23 C. Bommier, D. Leonard, Z. Jian, W. F. Stickle, P. A. Greaney and X. Ji, *Adv. Mater. Interfaces*, 2016, **3**, 1600449.
24 H. Lei, J. Li, X. Zhang, L. Ma, Z. Ji, Z. Wang, L. Pan, S. Tan and W. Mai, *InfoMat*, 2022, **4**, e12272.
25 H. Zheng, Q. Qu, L. Zhang, G. Liu and V. S. Battaglia, *RSC Adv.*, 2012, **2**, 4904–4912.
26 G. Foran, D. Mankovsky, N. Verdier, D. Lepage, A. Prébé, D. Aymé-Perrot and M. Dollé, *Iscience*, 2020, **23**, 113876.
27 A. Marojević, T. Pavčnik, O. Lužanin, J. Grdadolnik, K. Pirnat, A. Ponrouch, R. Dominko and J. Bitenc, *Batter. Supercaps*, 2025, 202500497.
28 H. Jia, J.-M. Kim, P. Gao, Y. Xu, M. H. Engelhard, B. E. Matthews, C. Wang and W. Xu, *Angew. Chem.*, 2023, **135**, e202218005.
29 G.-C. Chung, H.-J. Kim, S.-I. Yu, S.-H. Jun, J.-w. Choi and M.-H. Kim, *J. Electrochem. Soc.*, 2000, **147**, 4391.
30 W. Du, X. Jiang and L. Zhu, *J. Mater. Chem. A*, 2013, **1**, 10592–10606.
31 S. Flandrois and B. Simon, *Carbon*, 1999, **37**, 165–180.
32 H. Xiang, C. Chen, J. Zhang and K. Amine, *J. Power Sources*, 2010, **195**, 604–609.
33 L. Wu, D. Buchholz, C. Vaalma, G. A. Giffin and S. Passerini, *ChemElectroChem*, 2016, **3**, 292–298.

34 N. Nieto, J. Porte, D. Saurel, L. Djuandhi, N. Sharma, A. Lopez-Urionabarrenechea, V. Palomares and T. Rojo, *ChemSusChem*, 2023, **16**, e202301053.
35 L. Rakhymbay, N. Bazybek, K. Kudaibergenov, S.-T. Myung, Z. Bakenov and A. Konarov, *J. Power Sources*, 2024, **602**, 234347.
36 X. Dou, I. Hasa, M. Hekmatfar, T. Diemant, R. J. Behm, D. Buchholz and S. Passerini, *ChemSusChem*, 2017, **10**, 2668–2676.
37 X.-S. Wu, X.-L. Dong, B.-Y. Wang, J.-L. Xia and W.-C. Li, *Renewable Energy*, 2022, **189**, 630–638.
38 C. M. Ghimbeu, B. Zhang, A. M. de Yuso, B. Réty and J.-M. Tarascon, *Carbon*, 2019, **153**, 634–647.
39 J. Khedari, N. Nankongnab, J. Hirunlabh and S. Teekasap, *Build. Environ.*, 2004, **39**, 59–65.
40 P. Muensri, T. Kunanopparat, P. Menut and S. Siriwattanayotin, *Composites, Part A*, 2011, **42**, 173–179.
41 C. Moretti, B. Corona, R. Hoefnagels, I. Vural-Gürsel, R. Gosselink and M. Junginger, *Sci. Total Environ.*, 2021, **770**, 144656.
42 W. E. Tenhaeff, O. Rios, K. More and M. A. McGuire, *Adv. Funct. Mater.*, 2014, **24**, 86–94.
43 W. Zhang, J. Yin, Z. Lin, H. Lin, H. Lu, Y. Wang and W. Huang, *Electrochim. Acta*, 2015, **176**, 1136–1142.
44 Z. Yang, H. Guo, F. Li, X. Li, Z. Wang, L. Cui and J. Wang, *J. Energy Chem.*, 2018, **27**, 1390–1396.
45 Y.-F. Du, G.-H. Sun, Y. Li, J.-Y. Cheng, J.-P. Chen, G. Song, Q.-Q. Kong, L.-J. Xie and C.-M. Chen, *Carbon*, 2021, **178**, 243–255.
46 D. G. Kizzire, V. García-Negrón, D. P. Harper and D. J. Keffer, *ChemistryOpen*, 2022, **11**, e202100220.
47 C. M. Ghimbeu, B. Zhang, A. M. de Yuso, B. Réty and J.-M. Tarascon, *Carbon*, 2019, **153**, 634–647.
48 D. G. Kizzire, A. M. Richter, D. P. Harper and D. J. Keffer, *ACS Omega*, 2021, **6**, 19883–19892.
49 V. García-Negrón, D. G. Kizzire, O. Rios, D. J. Keffer and D. P. Harper, *Carbon*, 2020, **161**, 856–869.
50 R. Muzyka, E. Misztal, J. Hrabak, S. W. Banks and M. Sajdak, *Energy*, 2023, **263**, 126128.
51 H. Zhang, C. Chen, E. M. Gray and S. E. Boyd, *Biomass Bioenergy*, 2017, **105**, 136–146.
52 Y. Yan, G. Chen, W. Liu, M. Qu, Z. Xie and F. Wang, *J. Energy Storage*, 2024, **104**, 114590.
53 M. Ferreira, M. Costa, I. Mendes, M. Drumond, D. Piló-Veloso and N. Fernandes, *Cryst. Struct. Commun.*, 1998, **54**, 837–840.
54 K. Sears, A. Beelik, R. Casebier, R. Engen, J. Hamilton and H. Hergert, *J. Polym. Sci.*, 1971, 425–443.
55 T. P. Nguyen and J. H. Shim, *Phys. Chem. Chem. Phys.*, 2016, **18**, 13888–13896.
56 L. Mtemeri and Y. Qi, *EES Batteries*, 2026, **2**, 189–198.
57 M. Han, Z. Yi, W. Jia, F. Su, X. Li, C. Chen, P. Han and Z. Zuo, *ChemistrySelect*, 2025, **10**, e202500679.
58 A. Barreiro, F. Börrnert, S. M. Avdoshenko, B. Rellinghaus, G. Cuniberti, M. H. Rümmeli and L. M. Vandersypen, *Sci. Rep.*, 2013, **3**, 1115.
59 D. Vural, *Eur. Biophys. J.*, 2024, **53**, 405–414.
60 W. Zhan, K. Li, R. Khanna, Y. Konyukhov, Z. Liang, Y. Bu, Z. Sun, C. Jiang and J. Zhang, *Sustainability*, 2024, **16**, 3419.
61 A. K. Sangha, L. Petridis, J. C. Smith, A. Ziebell and J. M. Parks, *Environ. Prog. Sustain. Energy*, 2012, **31**, 47–54.
62 C. H. Lee, J. Kim, J. Ryu, W. Won, C. G. Yoo and J. S.-I. Kwon, *Chem. Eng. J.*, 2024, **487**, 150680.
63 R. Car and M. Parrinello, *Phys. Rev. Lett.*, 1985, **55**, 2471.
64 M. D. Slater, D. Kim, E. Lee and C. S. Johnson, *Adv. Funct. Mater.*, 2013, **23**, 947–958.
65 P. Harris, *Philos. Mag.*, 2004, **84**, 3159–3167.
66 E. O. Eren, E. Senokos, Z. Song, B. Mondal, A. Perju, T. Horner, E. B. Yılmaz, E. Scoppola, P.-L. Taberna, P. Simon, *et al.*, *Mater. Horiz.*, 2025, **12**, 886–898.
67 B. Tratnik, N. Van de Velde, I. Jerman, G. Kapun, E. Tchernychova, M. Tomsic, A. Jamnik, B. Genorio, A. Vizintin and R. Dominko, *ACS Appl. Energy Mater.*, 2022, **5**, 10667–10679.
68 H. S. Nguyen and A. Latz, *Phys. Chem. Chem. Phys.*, 2023, **25**, 28196–28204.
69 G. Kresse and J. Furthmüller, *Phys. Rev. B*, 1996, **54**, 11169.
70 H. Euchner and A. Groß, *Phys. Rev. Mater.*, 2022, **6**, 040302.
71 G. Kresse and D. Joubert, *Phys. Rev. B*, 1999, **59**, 1758.
72 J. Li, Y. Peng, X. Tang, B. Liu, L. Bai and K. Zhou, *Appl. Surf. Sci.*, 2022, **579**, 152055.
73 A. Weerasinghe, A. Ramasubramaniam and D. Maroudas, *Mater. Res. Express*, 2018, **5**, 115603.
74 K. S. Lee, T.-H. Kwon, T. Park and M. S. Jeong, *Theory and Practice in Microbial Enhanced Oil Recovery*, Gulf Professional Publishing, 2020.
75 J. Yi, M. Jia, H. Ai and K. Du, *ACS Appl. Mater. Interfaces*, 2026, **18**, 12962–12973.
76 X. Chen, Y. Fang, J. Tian, H. Lu, X. Ai, H. Yang and Y. Cao, *ACS Appl. Mater. Interfaces*, 2021, **13**, 18914–18922.
77 Z. Zhao, H. Chen, W. Zhang, S. Yi, H. Chen, Z. Su, B. Niu, Y. Zhang and D. Long, *Mater. Adv.*, 2023, **4**, 835–867.
78 J. Azizi, A. Groß and H. Euchner, *Batter. Supercaps*, 2026, **9**, e202500382.
79 J. Azizi, A. Groß and H. Euchner, *ChemSusChem*, 2024, **17**, e202301493.
80 E. Olsson, G. Chai, M. Dove and Q. Cai, *Nanoscale*, 2019, **11**, 5274–5284.
81 E. Olsson, J. Cottom and Q. Cai, *Small*, 2021, **17**, 2007652.
82 B. G. Vieira, E. B. Barros, D. G. Vercosa, G. Samsonidze, A. G. S. Filho and M. S. Dresselhaus, *Phys. Rev. Appl.*, 2014, **2**, 014006.
83 A. Maiti, A. Svizhenko and M. Anantram, *Phys. Rev. Lett.*, 2002, **88**, 126805.
84 J. Yin, Y. S. Zhang, H. Liang, W. Zhang and Y. Zhu, *Mater. Rep.: Energy*, 2024, **4**, 100268.
85 Y. Jin, Z. Shi, T. Han, H. Yang, H. Asfaw, R. Gond, R. Younesi, P. Jönsson and W. Yang, *Processes*, 2023, **11**, 764.
86 A. Ito, Y. Wang, S. Irle, K. Morokuma and H. Nakamura, *J. Nucl. Mater.*, 2009, **390**, 183–187.
87 F. Wang, L. Chen, J. Wei, C. Diao, F. Li, C. Du, Z. Bai, Y. Zhang, O. I. Malyi, X. Chen, *et al.*, *Energy Environ. Sci.*, 2025, **18**, 4312–4323.

88 J. Zhang, X. Wang, J. Hou, X. Li, M. Li, W. Zhao and N. He, *Sci. Total Environ.*, 2024, **944**, 173766.
89 L. Kitsu Iglesias, E. N. Antonio, T. D. Martinez, L. Zhang, Z. Zhuo, S. J. Weigand, J. Guo and M. F. Toney, *Adv. Energy Mater.*, 2023, **13**, 2302171.
90 J. M. Stratford, P. K. Allan, O. Pecher, P. A. Chater and P. Grey, *Chem. Commun.*, 2016, **52**, 12430–12433.
91 Y. Fujii, H. Yoshimo, R. Tatara, Z. T. Gossage, A. Koizumi and S. Komaba, *ACS Appl. Energy Mater.*, 2025, **8**, 6577–6585.
92 X. Wu, J. Jiang, C. Wang, J. Liu, Y. Pu, A. Ragauskas, S. Li and B. Yang, *Biofuels, Bioprod. Biorefin.*, 2020, **14**, 650–672.
93 S. Yang, L. Zhong, H. Li, X. Zu, F. Fu, Q. Liu, X. Qiu and W. Zhang, *Int. J. Biol. Macromol.*, 2025, 147017.
94 K.-L. Wu, W.-W. Zhang, T.-B. Jiang, M. Wu, W. Liu, H.-M. Wang and Q.-X. Hou, *Int. J. Biol. Macromol.*, 2023, **227**, 146–157.
95 S. Feng, Q. Ouyang, J. Huang, X. Zhang, Z. Ma, K. Liang and Q. Huang, *J. Renew. Mater.*, 2024, **12**, 1207.
96 L. Wang, S. Hao, J. Yao, Q. Liu, F. Fu, X. Zu, D. Yang, X. Qiu and W. Zhang, *J. Power Sources*, 2026, **665**, 239076.
97 J. Huang, W. Jian, L. Zhong, H. Li, Q. Liu, F. Fu, J. Wang, X. Zu, X. Qiu and W. Zhang, *Chem. Eng. Sci.*, 2026, **319**, 122343.
98 C. M. Ghimbeu, J. Górka, V. Simone, L. Simonin, S. Martinet and C. Vix-Guterl, *Nano energy*, 2018, **44**, 327–335.
99 A. Beda, F. Rabuel, M. Morcrette, S. Knopf, P.-L. Taberna, P. Simon and C. M. Ghimbeu, *J. Mater. Chem. A*, 2021, **9**, 1743–1758.
100 C.-W. Tai, W.-Y. Jao, L.-C. Tseng, P.-C. Wang, A.-P. Tu and C.-C. Hu, *J. Mater. Chem. A*, 2023, **11**, 19669–19684.